

# Importance of Interfacial Structures in the Catalytic Effect of Transition Metals on Diamond Growth

Jeong Woo Yang, Jong Hwan Park, Min Gyo Byun, Nong Moon Hwang, Jinwoo Park, and Byung Deok Yu\*

Cite This: *ACS Omega* 2021, 6, 28432–28440

Read Online

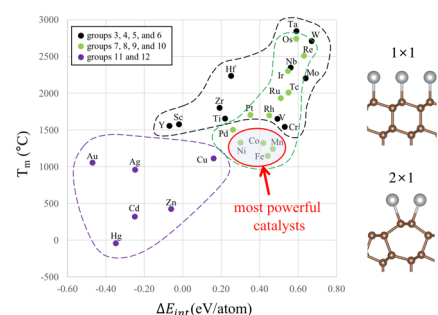
ACCESS |

Metrics & More

Article Recommendations

**ABSTRACT:** Here, using ab initio calculations, we investigated the interaction between transition metals (M) and diamond C(111) surfaces. As a physical parameter describing the catalytic effect of a transition metal on diamond growth, we considered interfacial energy difference,  $\Delta E_{\text{int}}$ , between  $1 \times 1$  and  $2 \times 1$  models of M/C(111). The results showed that the transition-metal elements in the middle of the periodic table (groups 4–10) favor a  $1 \times 1$  M/C(111) structure with diamond bulk-like interfaces, while the elements at the sides of the periodic table (groups 3, 11, and 12) favor a  $2 \times 1$  M/C(111) structure with the  $2 \times 1$  Pandey chain structure of C(111) underneath M. In addition, calculations of MC carbide formation for early transition metals (groups 3–6) showed that they have a tendency to form MC rather than M/C(111), which explains their low efficiency as catalysts for diamond growth. Further analysis suggests that  $\Delta E_{\text{int}}$  could serve as another parameter (catalytic descriptor) for describing catalytic diamond growth in addition to the conventional parameter of the melting temperature of M.

Scatter plot of the interface energy difference ( $\Delta E_{\text{int}}$ ) and the melting temperature ( $T_m$ ) for catalytic growth of diamond.



## 1. INTRODUCTION

Since General Electric successfully synthesized diamond for the first time in 1955<sup>1</sup> using a high-pressure and high-temperature method, growth of diamond has attracted considerable interest due to the importance for machine tools, optical coatings, high-temperature electronics, and next-generation power devices.<sup>2–8</sup> Diamond has been synthesized by using metal catalysts, such as Fe, Co, and Ni;<sup>9</sup> until recently, these transition metals were considered essential to catalytic diamond synthesis.<sup>10–16</sup>

During the synthesis process, the metal catalysts liquify. When the transition metals are catalytically activated, the melting temperature ( $T_m$ ) associated with carbon solubility is considered an important parameter to describe their catalytic efficiency. Most conventional catalysts showed a catalytic effect in the liquid phase around their  $T_m$ . However, Kanda et al.<sup>17</sup> reported that Cu (Zn) also had a catalytic effect at a much higher temperature than its  $T_m$ . Hence,  $T_m$  alone is insufficient to explain the catalytic power of transition metals.

Therefore, it is necessary to investigate the physical properties associated with metal adsorption on diamond surfaces to extract an additional parameter that explains the catalytic effect of transition metals. Among the low-index surfaces of diamond, as the most stable surface, C(111) plays an important role in determining the morphology of the growing diamond.<sup>18–22</sup> Regarding the stable surface structure

of clean C(111), although the details of the atomic structure remain controversial, most experimental and theoretical studies<sup>23,24</sup> support Pandey's  $2 \times 1$   $\pi$ -bonded chain model. The  $sp^2$   $\pi$ -bonded surface structure of the Pandey chain model would prevent incoming surface C atoms from forming  $sp^3$  bonds and thus diamond bulk-like films. As a result, the growth of graphite rather than diamond would be favorable. Therefore, in a high-pressure and high-temperature process, without catalytic metals, extreme conditions<sup>25</sup> of approximately 125 kbar and 3000 K are required due to the need to deform the strong surface  $\pi$ -bonds.

In the context of thin-film growth, many studies have been conducted on surface elements that remove the  $\pi$ -bonds of Pandey chains on C(111) through surface reactions.<sup>26–29</sup> Recently, we theoretically investigated the microscopic role of a Ni metal catalyst on C(111) through ab initio electronic and vibrational calculations.<sup>30,31</sup> The results showed that the addition of Ni induces the formation of a thermodynamically stable Ni–C interface with an  $sp^3$ -like  $1 \times 1$  diamond bulk-like

Received: September 10, 2021

Accepted: October 1, 2021

Published: October 13, 2021



structure, which is more favorable for diamond growth than an  $sp^2$ -like  $2 \times 1$  Pandey chain structure. This structural change is well represented by the interfacial energy difference between the  $1 \times 1$  and  $2 \times 1$  models. The more positive the interfacial energy difference, the more favorable the  $1 \times 1$  diamond bulk-like interfacial structure. The interfacial energy difference for Ni/C(111) was 0.30 eV/atom, which is much larger than the corresponding value ( $-0.78$  eV/atom) of the surface energy difference between the  $1 \times 1$  and  $2 \times 1$  models of C(111). Further kinetic calculations revealed that a carbon adatom, which is a source of diamond growth, can penetrate into a subsurface site to form a C–C bond. As a result, the catalytic Ni atoms enable surfactant-mediated processes for continuous growth of diamond. These reactive behaviors of Ni metals on C(111) shed light on the microscopic mechanism underlying the surface catalytic effect of Ni on diamond synthesis.

In the present work, we studied the catalytic effect of transition metals by carrying out ab initio total energy and electronic structure calculations of transition-metal (M)/C(111) based on the density functional theory (DFT),<sup>32,33</sup> which extends our earlier work<sup>30,31</sup> to other transition metals. We examined energetics, structural and electronic properties, and metal carbide formation of M on C(111) and obtained characteristic features that are very important for understanding the microscopic mechanism by which transition metals catalyze diamond growth.

## 2. COMPUTATION METHOD

All calculations were carried out using the plane-wave method within the framework of spin-unpolarized DFT, as implemented in the Vienna ab initio simulation package.<sup>34,35</sup> For the exchange–correlation interactions of electrons, we used the Perdew–Burke–Ernzerhof expression within the generalized-gradient approximation.<sup>36</sup> The electron–ion interactions were described using the projector augmented-wave method.<sup>37</sup> The electronic wave functions were expanded on a plane wave basis set with an energy cutoff of 400 eV.

For the calculations of the M-terminated C(111) surfaces, we used a supercell with a repeating slab structure consisting of six atomic C layers with a 20 Å thick vacuum region along the surface normal direction and a  $2 \times 1$  rectangular surface unit cell in the lateral ( $x$  and  $y$ ) directions. Figure 1 shows the atomic structures of M/C(111) with the  $1 \times 1$  and  $2 \times 1$  models used in this study, which have the  $1 \times 1$  and  $2 \times 1$  surface periodicity of C(111) underneath the M layer, respectively. For both models, we used the  $2 \times 1$  rectangular surface unit cell to facilitate comparative analysis. The number of M atoms per  $2 \times 1$  surface unit cell was 2, which corresponds to 1 monolayer (ML) of M surface coverage.

The M layer in M/C(111) was adsorbed only on the upper side of the slab, and the dangling bonds of the bottom C atoms of the slab were passivated with hydrogen atoms. For the slab, we used the theoretical equilibrium lattice constant of diamond in bulk ( $a_0 = 3.55$  Å). We used  $k$ -point integration with a  $6 \times 10 \times 1$  grid in the Brillouin zone of the supercell. To determine the positions of the H atoms in M/C(111), we used a two-sided surface of H-terminated C(111) [H/C(111)]; only the geometry of the H atoms was optimized. The obtained C–H distance was used to determine the bottom H-terminated surface. All M and C atoms were fully relaxed, except for the bottommost C and H atoms. Note that for the metals toward the left-hand side of the periodic table (Sc, Ti, V, Y, Zr, and Hf), their  $1 \times 1$  and  $2 \times 1$  M/C(111) interfaces tend to form

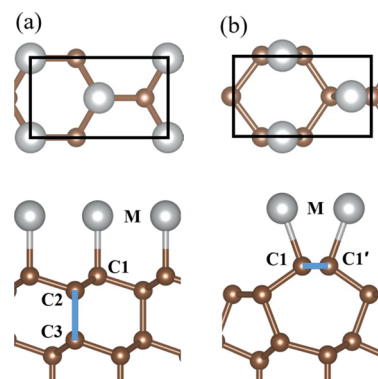


**Figure 1.** Top and side views of transition-metal (M)/C(111) surfaces. (a) Diamond bulk-like  $1 \times 1$  and (b) Pandey chain  $2 \times 1$  models. Large gray and small brown circles represent M and carbon atoms, respectively, where  $C_n$  denotes a carbon atom in the  $n$ -th carbon layer. The  $2 \times 1$  surface unit cell is denoted by the black lines. The two important C–C bonds in M/C(111) (C2–C3 in the  $1 \times 1$  model and C1–C1' in the  $2 \times 1$  model) are denoted by the blue lines.

structures that deviate from the M/C(111) interface structures shown in Figure 1, which were obtained for the other metal atoms. To extract meaningful features from interactions between the surface M atoms and the C(111) substrate atoms, we restricted the relaxation of those left-side metals to the structures shown in Figure 1, where the metals were relaxed only along the surface-normal ( $z$ ) direction, with their lateral atomic positions fixed to those in Figure 1. The restricted relaxation of the left-side metals does not affect the conclusions derived from this work because of the more favorable formation of metal carbides rather than M/C(111) for these metals. We continued the geometry optimization until the remaining forces of the atoms were smaller than 0.02 eV/Å.

The spin polarization effect was also tested for the effective diamond catalysts of Mn, Fe, Co, and Ni. The spin-polarized calculation results showed small changes in the interfacial energy differences between the  $1 \times 1$  and  $2 \times 1$  models of M/C(111), as compared with the corresponding values of the interfacial energy differences we obtained with the spin-unpolarized calculations. The variation in the interfacial energy differences with spin polarization was less than 0.07 eV/atom, which is much smaller than the spin-unpolarized calculation values of the interfacial energy differences in the range from 0.30 to 0.47 eV/atom. Therefore, spin polarization does not affect the conclusions derived in this paper.

For more detailed analysis of the interactions of the M atoms with C(111), we performed projected crystal orbital Hamiltonian population (pCOHP) analysis,<sup>38,39</sup> which is a partitioning scheme of the Kohn–Sham band structure energy in the plane-wave DFT calculations in terms of orbital-pair contributions. For this, we used the Local-Orbital Basis Suite Towards Electronic-Structure Reconstruction package.<sup>40</sup> The bond-analytical pCOHP provides quantitative information on the bonding, nonbonding, and antibonding contributions in the plane-wave DFT calculations.

## 3. RESULTS

**3.1. Interfacial Energy.** To determine the relative stability of the  $1 \times 1$  and  $2 \times 1$  M/C(111) interfaces, we calculated the interfacial energy difference per surface M atom of a  $1 \times 1$  surface unit cell ( $\Delta E_{\text{int}}$  in eV/atom) between the two

3	4	5	6	7	8	9	10	11	12
Sc	Ti	V	Cr	Mn	Fe	Co	Ni	Cu	Zn
-0.02	0.22	0.49	0.53	0.47	0.44	0.42	0.30	0.16	-0.05
Y	Zr	Nb	Mo	Tc	Ru	Rh	Pd	Ag	Cd
-0.07	0.19	0.56	0.64	0.55	0.51	0.46	0.26	-0.25	-0.25
	Hf	Ta	W	Re	Os	Ir	Pt	Au	Hg
	0.25	0.59	0.68	0.63	0.60	0.55	0.36	-0.47	-0.35

**Figure 2.** Interfacial energy difference ( $\Delta E_{\text{int}}$  in eV/atom) between the  $1 \times 1$  and  $2 \times 1$  models of the transition-metal (M)/C(111) surface,  $\Delta E_{\text{int}} = (E_{\text{M/C(111)}}^{2 \times 1} - E_{\text{M/C(111)}}^{1 \times 1})/2$ . Blue (orange) indicates  $1 \times 1$  ( $2 \times 1$ )-stable elements with positive (negative)  $\Delta E_{\text{int}}$ .

interfaces for each transition-metal element as follows:  $\Delta E_{\text{int}} = (E_{\text{M/C(111)}}^{2 \times 1} - E_{\text{M/C(111)}}^{1 \times 1})/2$ , where  $E_{\text{M/C(111)}}^{2 \times 1}$  and  $E_{\text{M/C(111)}}^{1 \times 1}$  are the total energies of the  $2 \times 1$  and  $1 \times 1$  M/C(111) interfaces, respectively. In Figure 2, we show the values of  $\Delta E_{\text{int}}$  in the form of a periodic table; under the convention used, a more positive value of  $\Delta E_{\text{int}}$  is more favorable for the formation of the  $1 \times 1$  M/C(111) structure.

In Figure 2, the elements that are stable for  $1 \times 1$  ( $2 \times 1$ ) M/C(111) interface structures are in blue (orange). The  $1 \times 1$  model is generally stable for elements nearer the middle of the periodic table, while the  $2 \times 1$  model is stable for those at the sides. As we move from the side to the middle, the  $1 \times 1$  model becomes more stable, as indicated by the deeper blue color; it is most stable for the group 6 elements. For each group, except groups 4 and 10, as we move down the periodic table, the values of  $\Delta E_{\text{int}}$  are larger in absolute value, and the difference in  $\Delta E_{\text{int}}$  values between the middles and sides increases.

Looking at the  $\Delta E_{\text{int}}$  results, the interfaces of the conventional catalytic elements of groups 8–10 (Fe, Co, Ni, Ru, Rh, Pd, Os, Ir, and Pt) have a stable  $1 \times 1$  structure with  $\Delta E_{\text{int}}$  in the range of 0.26–0.60 eV/atom. The middle elements of groups 6 and 7 (Cr, Mn, Mo, Tc, W, and Re) also have a stable  $1 \times 1$  interface structure, with  $\Delta E_{\text{int}}$  in the range of 0.47–0.68 eV/atom. The elements of groups 4 and 5 (Ti, V, Zr, Nb, Hf, and Ta) have a stable  $1 \times 1$  interface structure with  $\Delta E_{\text{int}}$  in the range of 0.19–0.59 eV/atom. The elements of group 3 (Sc and Y) have a slightly stable  $2 \times 1$  structure, with  $\Delta E_{\text{int}}$  values of  $-0.02$  and  $-0.07$  eV/atom, respectively. In groups 11 and 12, except for Cu, most elements have a stable  $2 \times 1$  interface structure with  $\Delta E_{\text{int}}$  in the range of  $-0.47$  to  $-0.05$  eV/atom. Note that all these values are more positive than the energy difference of  $-0.78$  eV/atom between the  $1 \times 1$  and  $2 \times 1$  models of clean C(111). We expect very weak catalytic effects for Cu and Zn. Cu is the only element in this group that has a positive  $\Delta E_{\text{int}}$  value (0.16 eV/atom); this is smaller than those of the conventional catalytic elements, suggesting that Cu will have a weak catalytic effect as compared with the conventional catalytic elements.

**3.2. Structures.** Next, we investigated structural changes induced by the adsorption of M atoms on C(111). Our previous studies<sup>30,31</sup> demonstrated that surface Ni adsorption on C(111) favors a diamond bulk-like  $1 \times 1$  interface structure. In this  $1 \times 1$  Ni/C(111) structure, compared to the clean  $1 \times 1$  C(111), the C1–C2 bond is elongated, the C2–C3 bond is shortened, and  $\angle(\text{C1–C2–C3})$  has a value ( $107.7^\circ$ ) close to that of bulk diamond ( $109.5^\circ$ ). The shortened C2–C3 bond inhibits the C1–C2 bilayer from exfoliating to become a graphene layer. In the  $2 \times 1$  Ni/C(111) structure, compared to

that of clean  $2 \times 1$  C(111), the C1–C1' bond is elongated by the Ni adsorption. Thus, the Ni-induced structural changes well explain the formation of  $\text{sp}^3$ -bonded carbon in the  $1 \times 1$  Ni/C(111) structure as well as the weakening of the  $\pi$ -bonds of the surface C atoms in the Pandey chain structure of  $2 \times 1$  Ni/C(111). Therefore, we analyzed the structural changes in terms of two important bond lengths: C2–C3 in the  $1 \times 1$  model and C1–C1' in the  $2 \times 1$  model. These bonds are indicated by blue lines in the lower panels of Figure 1.

Figure 3a shows the C2–C3 bond length in  $1 \times 1$  M/C(111). Moving from left to right in each row of the periodic table, the length decreases and then increases. Compared to the elements at the sides of the periodic table, the C2–C3 bonds of the elements in the middle are much shorter and thus closer to the bond length (1.54 Å) in the bulk diamond, with the values for the group 7 elements being closest to that of bulk diamond. As we go down the periodic table for each group, for the elements in the middle, the C2–C3 bond lengths become much closer to that of the bulk diamond structure, whereas for the elements in groups 3 and 4, they show only very small changes. The elements in groups 11 and 12 have larger values than that of bulk diamond.

Figure 3b shows the variation in the C1–C1' bond length in  $2 \times 1$  M/C(111). Moving from left to right in each row of the periodic table, the length increases and then decreases. Compared to the elements at the sides of the periodic table, the C1–C1' bonds are longer for elements in the middle than for the Pandey  $\pi$ -bonded chain structure of C(111) (1.44 Å). Moving down the periodic table for each group, for the elements in the middle, the C1–C1' bonds are longer than those of clean  $2 \times 1$  C(111), whereas for the elements in groups 3, 11, and 12, the C1–C1' bond lengths are closer to that in clean  $2 \times 1$  C(111). Finally, for the elements in groups 4 and 5, the variation in C1–C1' bond length is small.

These structural features are strongly associated with the  $\Delta E_{\text{int}}$  results. Our structural analysis clearly shows that middle elements have a more  $\text{sp}^3$ -like interfacial structure, close to that of diamond bulk, whereas the side elements have a more  $\text{sp}^2$ -like interfacial structure, close to the  $\text{sp}^2$  surface structure of clean  $2 \times 1$  C(111). This agrees well with the results for  $\Delta E_{\text{int}}$ .

**3.3. M–C Cleavage Energy.** Next, we investigated the interaction between M layers and the carbon substrate. Figure 4a,b shows the M–C cleavage energy of the  $1 \times 1$  and  $2 \times 1$  models of M/C(111), respectively. This is the energy necessary to cleave the M overlayer from the C(111) substrate, calculated as follows:

$$E_{\text{M–C}} = [E_{\text{M}}^{\text{layer}} + E_{\text{C(111)}}] - E_{\text{M/C(111)}}$$



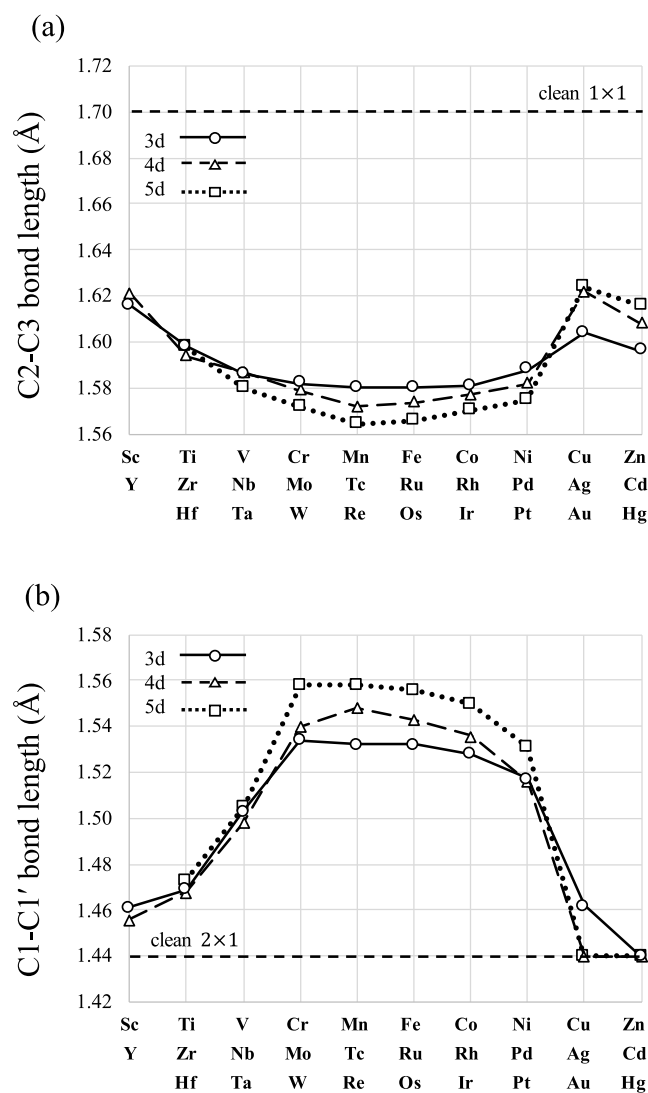


**Figure 3.** (a) C2–C3 bond length in  $1 \times 1$  transition-metal (M)/C(111) and (b) C1–C1' bond length in  $2 \times 1$  transition-metal (M)/C(111).

where  $E_M^{\text{layer}}$  and  $E_{\text{C}(111)}$  are the total energies of the isolated M layer and the C(111) frozen to M/C(111), respectively.

Compared to the side elements, the middle elements have a higher M–C cleavage energy and so can gain energy via the formation of an M–C bond. Moving down the periodic table of each group, the effect of the M–C interaction becomes much stronger in the middle and weaker at the sides, and the difference in  $E_{\text{M–C}}$  between the middle and side elements increases. Also, the  $1 \times 1$  model has a higher overall M–C interaction energy than the  $2 \times 1$  model (Figure 4a,b), indicating that more energy is gained from M–C bond formation in the  $1 \times 1$  than  $2 \times 1$  model. This trend in the change of energy is very strongly associated with the structural changes of the subsurface C atoms because M–C bond formation causes subsurface electron rearrangement and changes in the subsurface structure (Figures 3 and 4). This indicates that the stronger the M–C bond, the more stable the  $sp^3$ -like interfacial structure.

**3.4. Electronic Structure.** To obtain greater insight into the energetic and structural changes induced by the adsorption

of M atoms on C(111), we investigated the electronic structure of the M/C(111) surfaces.

We first analyzed the interactions between the M layer and underlying C(111) substrate by examining the electronic structures of the isolated M layer frozen to M/C(111) and clean C(111). Figure 5a shows the calculated projected electronic densities of states of the  $3d_{z^2}$  bands of the isolated M layers frozen to the  $1 \times 1$  M/C(111) for selected 3d transition metals. The black horizontal line indicates the peak position of the  $2p_z$  band of the surface C1 atom of  $1 \times 1$  clean C(111) at  $-4.70$  eV with respect to the vacuum energy level. Note that the  $3d_{z^2}$  band moves down with respect to the vacuum energy level from left to right along each row of the periodic table. The peak position of the  $3d_{z^2}$  band is closest to the black horizontal line for Mn, which is in group 7; therefore, the interaction between the  $3d_{z^2}$  and  $2p_z$  states is the strongest for Mn. In the  $2 \times 1$  system (Figure 5b), the interactions of the metal  $3d_{z^2}$  band with both the  $\pi$  and  $\pi^*$  peaks of the  $2p_z$  bands of surface C1 and C1' atoms of  $2 \times 1$  clean C(111) are important. The average position of the  $\pi$  and  $\pi^*$  peaks is located at  $-4.82$  eV with respect to the vacuum energy level; this is closest to the peak positions of the  $3d_{z^2}$  bands of the middle elements, such as Mn. Therefore, we expect that the interaction between the M layer and  $2 \times 1$  C(111) would also be the strongest for the middle elements. These results explain why the M–C cleavage energy is the largest for the middle elements in each row of the periodic table.

In addition, the strength of the M–C bond can be analyzed by calculating the pCOHP.<sup>41,42</sup> Figure 6a,b shows the calculated  $-p\text{COHP}$  of the M–C bond in the  $1 \times 1$  and  $2 \times 1$  models of M/C(111), respectively; here, the positive (negative) values of  $-p\text{COHP}$  denote bonding (antibonding). Electron occupation increases from left to right in each row of the periodic table. At Sc (group 3), only the bonding states of the M–C bond are partially occupied; more bonding states are occupied until we reach Mn (group 7). For Mn, the bonding states are fully occupied, while the antibonding states are entirely unoccupied. After Mn, the antibonding states of the M–C bond are more occupied as we move to the right side in each row of the periodic table. Therefore, the M–C bond is the strongest for the middle elements, such as Mn in group 7, where electrons fully occupy the bonding states of that M–C bond. Interestingly, the  $1 \times 1$  model has a much stronger peak intensity than the  $2 \times 1$  model. This agrees with the characteristics of the M–C cleavage energy (Figure 4). This well explains the stronger M–C bond formation in the  $1 \times 1$  model compared to the  $2 \times 1$  model.

To gain insight into the charge rearrangement, we performed a charge analysis based on an isosurface plot of the electron density difference,  $\Delta\rho$ , for M/C(111) surfaces of selected 3d transition metals. We calculated this as  $\Delta\rho = \rho_{\text{M/C}(111)} - \rho_{\text{C}(111)} - \rho_{\text{M}}$ , where  $\rho_{\text{M/C}(111)}$ ,  $\rho_{\text{C}(111)}$ , and  $\rho_{\text{M}}$  are the electron densities of M/C(111); the frozen, clean C(111) surface without the M layer; and the isolated frozen M layer, respectively.

Figure 7a,b shows the isosurface plots of  $\Delta\rho$  for the selected M/C(111) surfaces in the  $1 \times 1$  and  $2 \times 1$  models, respectively. Substantial rearrangement of electrons around the surface atoms can be seen. In the  $1 \times 1$  model (Figure 7a), significant accumulation of electrons can be seen in the region between the M and C1 atoms in M/C(111). The adsorption of the M atom on C(111) removes the dangling bond of the C1 atom and forms the covalent-like M–C1 bond. In addition,

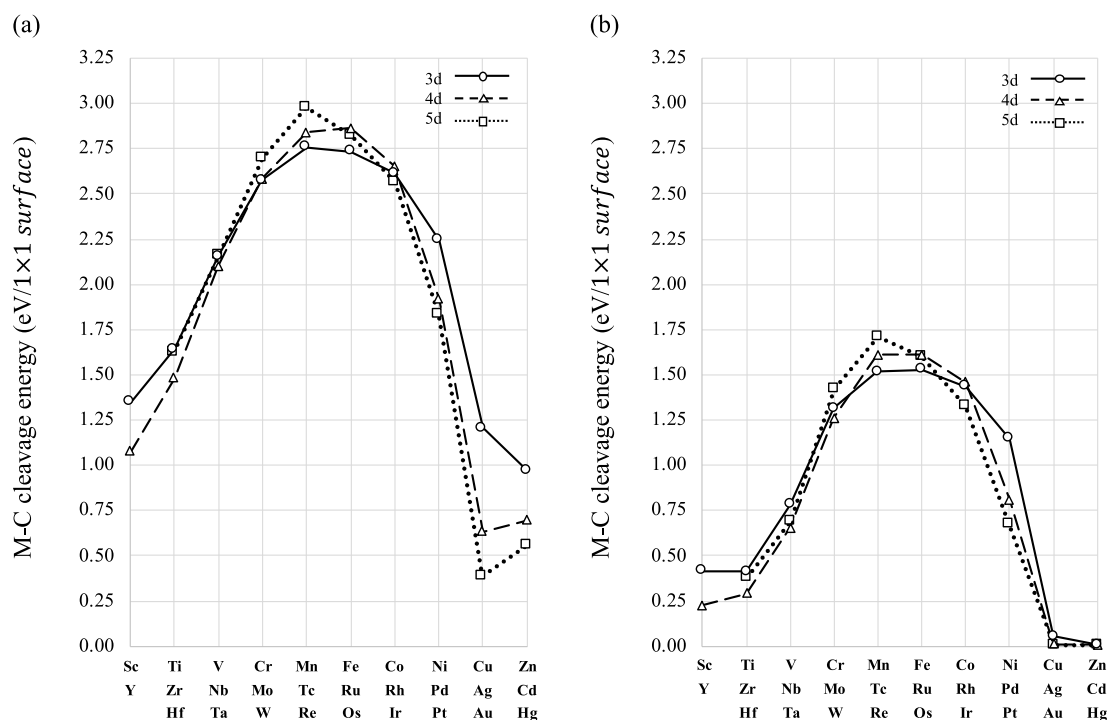


**Figure 4.** Transition-metal (M)–C cleavage energies of the (a)  $1 \times 1$  and (b)  $2 \times 1$  models in M/C(111).

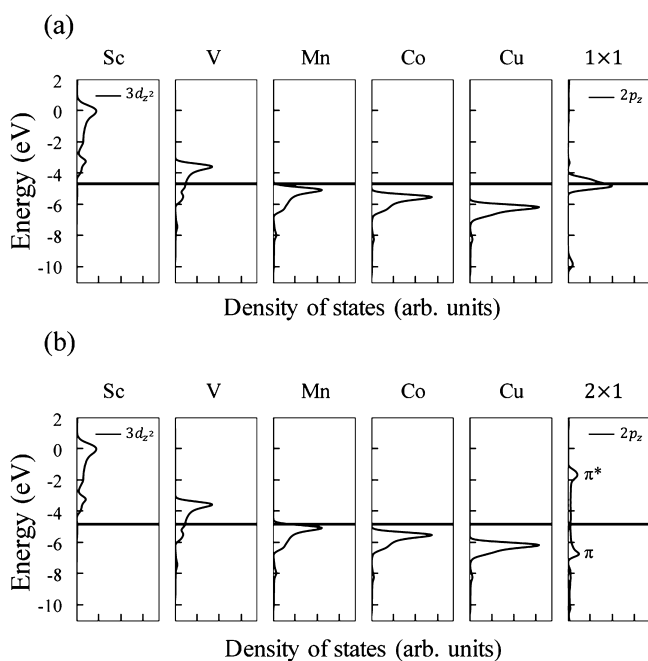


**Figure 5.** Projected electronic density of states for the  $3d_{z^2}$  band of the isolated transition-metal layers frozen to the transition-metal (M)/C(111) in the (a)  $1 \times 1$  and (b)  $2 \times 1$  models. The panel in the last column of (a) [(b)] shows the  $2p_z$  band of the surface C1 atom (C1 and C1' atoms) of geometry-optimized clean C(111) in the  $1 \times 1$  ( $2 \times 1$ ) model. The black horizontal lines in (a,b) indicate the peak position of the  $2p_z$  band of the C1 atom in  $1 \times 1$  clean C(111) at  $-4.70$  eV, and the average position of the  $\pi^*$ - and  $\pi$ -state peaks of the C1 and C1' atoms in  $2 \times 1$  clean C(111) at  $-4.82$  eV, respectively. Zero energy is set at the vacuum energy level.

electron accumulation occurs in the region between the C2 and C3 atoms, which is responsible for the hardening of the C2–C3 bond. Figure 7a shows greater electron

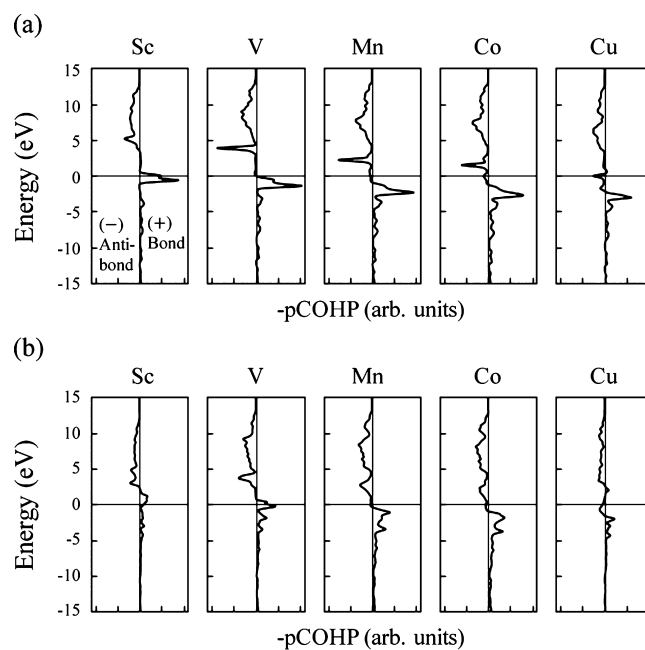


**Figure 6.** Projected crystal orbital Hamilton population (pCOHP) analysis of the transition-metal M( $3d_{z^2}$ )–C( $2p_z$ ) bond of M/C(111) in the (a)  $1 \times 1$  and (b)  $2 \times 1$  models. The horizontal line at zero energy indicates the Fermi energy level of M/C(111). Bonding (antibonding) states have a positive (negative) value of  $-pCOHP$ .

in the region between the C2 and C3 atoms for the middle elements (V, Mn, and Co) than for the side elements (Sc and Cu); this is consistent with the structural result showing that the C2–C3 bond is shorter in the middle elements (Figure 3a). Under the  $2 \times 1$  model (Figure 7b), the M atom is bonded obliquely with the C1 or C1' atom on the surface and interacts covalently with the C1 or C1' atom by accumulating electrons in the region between the M and C1 or C1' atoms.

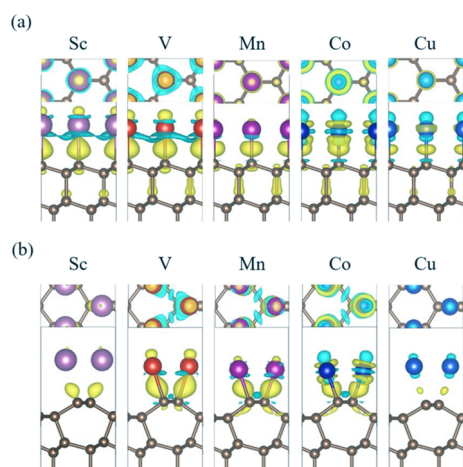


**Figure 7.** Isosurface plots of electron density difference, with top and side views of the transition-metal (M)/C(111) surfaces shown in the (a)  $1 \times 1$  and (b)  $2 \times 1$  models. Electron accumulation (depletion) regions are denoted by yellow (blue). The isosurface levels are  $\pm 0.007$  electrons/bohr<sup>3</sup>.

Interestingly, electron depletion occurs in the region above the C1–C1' bond for the middle elements (V, Mn, and Co) but not for the side ones (Sc and Cu). This electron depletion shows that severe weakening of the  $\pi$ -bonds of the C1 and C1' atoms occurs mainly for the middle elements (Figure 3b).

**3.5. Carbide Formation.** Because it is another important factor when selecting a catalytic metal for M/C(111), we also considered the tendency toward MC carbide formation. The MC carbide formation energy  $E_f^{\text{MC}}$  is defined as  $E_f^{\text{MC}} = E_{\text{MC}} - (E_{\text{M}} + \mu_{\text{C}})$ , where  $E_{\text{MC}}$ ,  $E_{\text{M}}$ , and  $\mu_{\text{C}}$  are the total energies of MC in the bulk, the M atom in the bulk metal, and the C atom in bulk graphite, respectively. It is well known that as we go to the left side in each row of the periodic table, MC carbide formation energies  $E_f^{\text{MC}}$  become lower, as compared with the other elements in each row of the periodic table, and thereby, MC carbide formation of the left-side elements becomes favorable.<sup>43,44</sup> This formation of carbide would prevent elements from forming M films on C(111) and therefore becoming potent diamond catalysts because much higher temperatures and pressures are required to dissolve these carbides. To determine the relative stability of M/C(111) with respect to the formation of MC, we calculated the relative film formation energy,  $\Delta E_f$ , of M per  $1 \times 1$  surface unit cell for  $1 \times 1$  M/C(111) as follows:  $\Delta E_f = [E_{\text{M/C(111)}} - (2\mu_{\text{M}} + E_{\text{C(111)}})]/2$ . Here, as the chemical potential,  $\mu_{\text{M}}$  of the M atom associated with the formation of MC, we used  $\mu_{\text{M}} = E_{\text{MC}} - \mu_{\text{C}}$ . The MC has a rock-salt structure, and its lattice constant was fully optimized. Figure 8 shows the  $\Delta E_f$  of metal M for  $1 \times 1$  M/C(111) with respect to the formation of rock-salt MC carbides. Note that before group 6, the formation of MC is more favorable than the formation of  $1 \times 1$  M/C(111); thus, the early transition metals, in groups 3–6, are less likely to form M/C(111) (needed for its catalytic effect) compared to those in groups 7–10.

#### 4. DISCUSSION: CATALYTIC EFFICIENCY DESCRIPTORS

We used DFT calculations to analyze the interfacial structures of M/C(111) and found that the middle elements (groups 4–10) favor the stable  $sp^3$ -like  $1 \times 1$  interfacial structure, while the side elements (groups 3, 11, and 12) favor the  $sp^2$ -like  $2 \times 1$

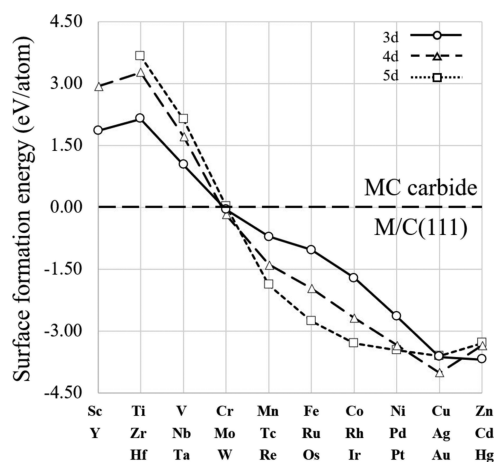


**Figure 8.** Film formation energy of the transition metal, M, per  $1 \times 1$  surface unit cell for  $1 \times 1$  M/C(111) with respect to the formation of rock-salt MC carbides. The positive (negative) values indicate favorable formation of MC [M films on C(111) with the structures of  $1 \times 1$  M/C(111)].

one. Further film formation energy calculations for carbide showed that the early transition metals (groups 3–6) easily form MC rather than the M layer on C(111), which is needed for catalysis.

Previously, the melting temperature ( $T_m$ ) of transition metals has been considered as the key factor for catalytic diamond synthesis.<sup>9</sup> However,  $T_m$  does not fully explain why Cu is a catalyst while Ag and Au do not, despite similar  $T_m$  values.<sup>17</sup> Therefore, to better understand the catalytic effect of metals, we introduced another parameter (catalytic descriptor),  $\Delta E_{\text{int}}$  to represent the catalytic effect of a transition metal.

Figure 9 shows a scatter plot for transition metals with two important parameters for diamond synthesis:  $T_m$  and  $\Delta E_{\text{int}}$

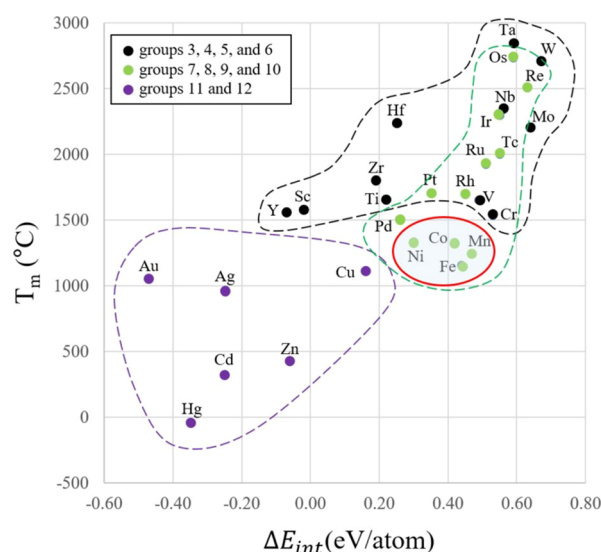


**Figure 9.** Scatter plot of two parameters for transition metals: experimental melting temperature ( $T_m$ ) and the interfacial energy difference ( $\Delta E_{\text{int}}$ ) between the  $1 \times 1$  and  $2 \times 1$  models of transition-metal (M)/C(111).  $T_m$  data are from ref 43. Black, green, and violet circles indicate the elements in groups 3–6, 7–10, and 11–12, respectively; the dotted curve of the corresponding color indicates the region of each group. The red circle indicates the most powerful catalytic metal elements for diamond growth.

between the  $1 \times 1$  and  $2 \times 1$  models of M/C(111). First, we shall consider the elements of groups 11 and 12 in the bottom-left part of Figure 9; these elements have lower  $T_m$  and  $\Delta E_{\text{int}}$  values than the others. However, despite their lower  $T_m$ , these elements have poor catalytic efficiency because of their lower  $\Delta E_{\text{int}}$  compared to the other transition metals. Note that among the elements of groups 11 and 12, Cu has the highest  $\Delta E_{\text{int}}$  value, which explains why it showed the best catalytic efficiency in the experiments conducted by Kanda et al. on Cu, Zn, and Au.<sup>17</sup> They also observed that Cu exhibited a catalytic effect at a much higher temperature than its  $T_m$ , different from conventional catalysts; therefore, they called this temperature the “reaction temperature”. We believe that the reaction temperature is associated with  $\Delta E_{\text{int}}$ , which we have proposed in this study for surface catalytic effects. Therefore, it is important to consider  $\Delta E_{\text{int}}$  in addition to  $T_m$ , which has previously been considered the key factor in catalytic diamond synthesis.

Second, we consider the elements of groups 7–10 in the top-right area of Figure 9; they have relatively higher  $T_m$  and  $\Delta E_{\text{int}}$  values than the elements of groups 11 and 12. Most of these elements are among the conventional catalysts identified by General Electric in 1955 when synthetic diamonds were first developed.<sup>1,9</sup> Note that among the elements, Mn, Fe, Co, and Ni (delineated in red in Figure 9) have the lowest  $T_m$  in groups 7–10, respectively; even today, these metals are the most powerful catalytic metal elements. More detailed experimental results for these four catalysts showed that Mn, Fe, Co, and Ni have diamond growth temperatures that decrease in that order, despite their similar  $T_m$ ,<sup>9,43,45</sup> interestingly, according to our calculations, they have M–C cleavage energies that also decrease in this order (Figure 4a). In our previous study,<sup>30</sup> we suggested that surfactant-mediated growth<sup>46–49</sup> occurs in the Ni/C(111) system, in which Ni atoms exchange their positions with incoming C atoms for continuous diamond growth, maintaining the  $1 \times 1$  M/C(111) structure. In this process, an M–C bond must be cleaved and a C–C bond is formed. Therefore, moderate M–C bond strength is important for diamond synthesis because it is kinetically advantageous for continuous diamond growth in M/C(111).

Last, the elements of groups 3–6 appear in the top-right area of Figure 9. Although these elements have similar  $T_m$  and  $\Delta E_{\text{int}}$  values to the elements of groups 7–10, these elements tend to form metal carbides rather than M/C(111). This carbide formation would prevent the metals from forming M films on C(111) and thus acting as powerful diamond catalysts. This finding coincides with the experimental results of Wakatsuki, that is, that the elements of groups 3–6 exhibit no catalytic behavior below 2000 °C.<sup>50</sup>


## 5. CONCLUSIONS

Using DFT, we calculated the interfacial energy difference,  $\Delta E_{\text{int}}$ , between  $1 \times 1$  and  $2 \times 1$  models of transition-metal (M)/C(111) surfaces, which is very important for understanding the catalytic effect of M during the growth of diamond on C(111). The results showed that the elements near the middle of the periodic table (groups 4–10) favor a stable  $1 \times 1$  M/C(111) structure with a diamond bulk-like structure at the interface, while the side elements near the sides of the periodic table (groups 3, 11, and 12) favor a  $2 \times 1$  M/C(111) structure with the  $2 \times 1$  Pandey chain model of C(111) underneath M. To obtain a detailed understanding of the interaction between the M layer and the C(111) substrate,

we also analyzed the atomic structures, M–C cleavage energies, and electronic properties. Further DFT calculations of the film formation of metal carbides showed that the early transition metals (groups 3–6) tend to form metal carbides rather than M/C(111). This behavior prevents these elements from forming an M film on C(111) and thus acting as powerful catalysts for diamond growth. Based on our calculations of M/C(111) with the  $1 \times 1$  and  $2 \times 1$  models, we herein proposed another parameter (catalytic descriptor),  $\Delta E_{\text{int}}$ , representing the surface catalytic effect, in addition to the melting temperature ( $T_m$ ) of transition metals, which has previously been considered the key parameter in catalytic diamond synthesis. A scatter plot using the two parameters predicted that Fe, Co, Ni, and Mn, which have medium  $\Delta E_{\text{int}}$  and  $T_m$  values, are the best catalytic metals for diamond growth, which agrees with experimental results. We expect that the microscopic catalysis mechanism for diamond growth proposed herein is also applicable to metal alloys, which could be used for catalytic diamond synthesis in the future.

## AUTHOR INFORMATION

### Corresponding Author

Byung Deok Yu – Department of Physics, University of Seoul, Seoul 02504, Republic of Korea;  [orcid.org/0000-0002-3948-8811](https://orcid.org/0000-0002-3948-8811); Email: [ybd@uos.ac.kr](mailto:ybd@uos.ac.kr)

### Authors

Jeong Woo Yang – Department of Materials Science and Engineering, Seoul National University, Seoul 08826, Republic of Korea

Jong Hwan Park – Department of Materials Science and Engineering, Seoul National University, Seoul 08826, Republic of Korea

Min Gyo Byun – Department of Materials Science and Engineering, Seoul National University, Seoul 08826, Republic of Korea

Ngong Moon Hwang – Department of Materials Science and Engineering, Seoul National University, Seoul 08826, Republic of Korea;  [orcid.org/0000-0003-1377-8658](https://orcid.org/0000-0003-1377-8658)

Jinwoo Park – Department of Physics, University of Seoul, Seoul 02504, Republic of Korea

Complete contact information is available at: <https://pubs.acs.org/10.1021/acsomega.1c05005>

### Notes

The authors declare no competing financial interest.

## ACKNOWLEDGMENTS

This work was partially supported by the Global Frontier Program through the Global Frontier Hybrid Interface Materials (GFHIM) of the National Research Foundation of Korea (NRF) funded by the Ministry of Science, ICT and Future Planning (MSIT) (no. NRF-2013M3A6B1078874), the National Research Foundation of Korea (NRF) grant funded by the Korea government (MSIT) (no. 2020R1A5A6017701), and the BK21PLUS SNU Materials Division for Educating Creative Global Leaders (21A20131912052).

## REFERENCES

- (1) Bundy, F. P.; Hall, H. T.; Strong, H. M.; Wentorfjun, R. H. Man-made diamonds. *Nature* **1955**, *176*, 51–55.
- (2) Achard, J.; Jacques, V.; Tallaire, A. Chemical vapour deposition diamond single crystals with nitrogen-vacancy centres: A review of



- material synthesis and technology for quantum sensing applications. *J. Phys. D: Appl. Phys.* **2020**, *53*, 313001.
- (3) Chen, Z.; Ma, D.; Wang, S.; Dai, W.; Zhu, P.; Zhu, Y.; Liu, B. Wear resistance and thermal stability enhancement of PDC sintered with Ti-coated diamond and cBN. *Int. J. Refract. Met. Hard Mater.* **2020**, *92*, 105278.
- (4) Hall, D. L.; Voss, L. F.; Grivickas, P.; Bora, M.; Conway, A. M.; Scajev, P.; Grivickas, V. Photoconductive switch with high sub-bandgap responsivity in nitrogen-doped diamond. *IEEE Electron Device Lett.* **2020**, *41*, 1070–1073.
- (5) Lai, H.; Stenzel, M. H.; Xiao, P. Surface engineering and applications of nanodiamonds in cancer treatment and imaging. *Int. Mater. Rev.* **2020**, *65*, 189–225.
- (6) Sha, X.; Yue, W.; Zhang, H.; Qin, W.; She, D.; Wang, C. Thermal stability of polycrystalline diamond compact sintered with boron-coated diamond particles. *Diamond Relat. Mater.* **2020**, *104*, 107753.
- (7) Trofimov, S. D.; Tarelkin, S. A.; Bolshedvorskii, S. V.; Bormashov, V. S.; Troshchiev, S. Y.; Golovanov, A. V.; Luparev, N. V.; Prikhodko, D. D.; Boldyrev, K. N.; Terentiev, S. A.; et al. Spatially controlled fabrication of single NV centers in Ila HPHT diamond. *Opt. Mater. Express* **2020**, *10*, 198–207.
- (8) Li, H.; Zhou, K.; Cao, J.; Wei, Q.; Lin, C.-T.; Pei, S. E.; Ma, L.; Hu, N.; Guo, Y.; Deng, Z.; et al. A novel modification to boron-doped diamond electrode for enhanced, selective detection of dopamine in human serum. *Carbon* **2021**, *171*, 16–28.
- (9) Bovenkerk, H. P.; Bundy, F. P.; Hall, H. T.; Strong, H. M.; Wentorf, R. H. Preparation of diamond. *Nature* **1959**, *184*, 1094–1098.
- (10) Chen, L.; Miao, X.; He, X.; Guo, L.; Fang, S.; Wang, Y.; Wang, Z.; Fang, C.; Ma, H.; Jia, X. Effects of Fe-Ni solvent with different Fe contents on the boron concentration in colorless diamonds. *J. Cryst. Growth* **2018**, *498*, 67–70.
- (11) Li, Y.; Wang, C.; Chen, L.; Guo, L.; Zhang, Z.; Fang, C.; Ma, H. An effective method to improve the growth rate of large single crystal diamonds under HPHT processes: optimized design of the catalyst geometric construction. *RSC Adv.* **2019**, *9*, 32205–32209.
- (12) Su, L.-X.; Zhao, C.-X.; Lou, Q.; Niu, C.-Y.; Fang, C.; Li, Z.; Shen, C.-L.; Zang, J.-H.; Jia, X.-P.; Shan, C.-X. Efficient phosphorescence from synthetic diamonds. *Carbon* **2018**, *130*, 384–389.
- (13) Fang, S.; Ma, H.; Wang, Z.; Yang, Z.; Cai, Z.-h.; Ding, L.; Miao, X.; Chen, L.; Jia, X. Study on growth characteristics of Ib-type diamond in an Fe-Ni-C-S system. *CrystEngComm* **2019**, *21*, 6010–6017.
- (14) Fang, C.; Shen, W.; Zhang, Y.; Mu, P.; Zhang, Z.; Jia, X. Si doping effects on the growth of large single-crystal diamond in a Ni-based metal catalyst system under high pressure and high temperature. *Cryst. Growth Des.* **2019**, *19*, 3955–3961.
- (15) Fang, S.; Wang, Y.; Chen, L.; Lu, Z.; Cai, Z.; Fang, C.; Zhao, Z.; Ma, H.; Jia, X. The effect of pressure on synthetic diamond crystals at high temperatures and pressures in an Fe/Ni catalyst system. *CrystEngComm* **2021**, *23*, 1406–1414.
- (16) Shevyrtalov, S.; Barannikov, A.; Palyanov, Y.; Khokhryakov, A.; Borzdov, Y.; Sergueev, I.; Rashchenko, S.; Snigirev, A. Towards high-quality nitrogen-doped diamond single crystals for X-ray optics. *J. Synchrotron Radiat.* **2021**, *28*, 104.
- (17) Kanda, H.; Akaiishi, M.; Yamaoka, S. New catalysts for diamond growth under high pressure and high temperature. *Appl. Phys. Lett.* **1994**, *65*, 784–786.
- (18) Larsson, K.; Tian, Y. Effect of surface termination on the reactivity of nano-sized diamond particle surfaces for bio applications. *Carbon* **2018**, *134*, 244–254.
- (19) Liu, Z.; Zheng, S.; Lu, Z.; Pu, J.; Zhang, G. Adhesive transfer at copper/diamond interface and adhesion reduction mechanism with fluorine passivation: A first-principles study. *Carbon* **2018**, *127*, 548–556.
- (20) Beck, R. A.; Petrone, A.; Kasper, J. M.; Crane, M. J.; Pauzuskie, P. J.; Li, X. Effect of surface passivation on nanodiamond crystallinity. *J. Phys. Chem. C* **2018**, *122*, 8573–8580.
- (21) Attrash, M.; Kuntumalla, M. K.; Michaelson, S.; Hoffman, A. Nitrogen terminated diamond (111) by RF (N<sub>2</sub>) plasma—chemical states, thermal stability and structural properties. *Surf. Sci.* **2021**, *703*, 121741.
- (22) Yan, B.; Chen, N.; He, N.; Wu, Y.; Zhang, X.; Li, L. Surface modeling and component analysis of picosecond laser ablation of CVD diamond. *Diamond Relat. Mater.* **2021**, *111*, 108191.
- (23) Pandey, K. C. New dimerized-chain model for the reconstruction of the diamond (111)-(2x1) surface. *Phys. Rev. B: Condens. Matter Mater. Phys.* **1982**, *25*, 4338–4341.
- (24) Himpsel, F. J.; Eastman, D. E.; Heimann, P.; van der Veen, J. F. Surface states on reconstructed diamond (111). *Phys. Rev. B: Condens. Matter Mater. Phys.* **1981**, *24*, 7270–7274.
- (25) Bundy, F. P. Direct conversion of graphite to diamond in static pressure apparatus. *J. Chem. Phys.* **1963**, *38*, 631–643.
- (26) Kern, G.; Hafner, J.; Kresse, G. Atomic and electronic structure of diamond (111) surfaces I. Reconstruction and hydrogen-induced de-reconstruction of the one dangling-bond surface. *Surf. Sci.* **1996**, *366*, 445–463.
- (27) Saito, M.; Oshiyama, A.; Miyamoto, Y. Atomic structure and phonons in the  $\pi$ -bonded chain of the clean diamond (111) surface. *Phys. Rev. B: Condens. Matter Mater. Phys.* **1998**, *57*, R9412–R9415.
- (28) Sandfort, B.; Mazur, A.; Pollmann, J. Surface phonons of hydrogen-terminated semiconductor surfaces. II. The H:C(111)-(1x1) system. *Phys. Rev. B: Condens. Matter Mater. Phys.* **1995**, *51*, 7150–7156.
- (29) Sen, F. G.; Qi, Y.; Alpas, A. T. Surface stability and electronic structure of hydrogen- and fluorine-terminated diamond surfaces: A first-principles investigation. *J. Mater. Res.* **2011**, *24*, 2461–2470.
- (30) Yang, J. W.; Park, J. H.; Byun, M. G.; Park, J.; Yu, B. D.; Hwang, N. M. Beyond-carbon-solvency effects of catalytic metal Ni on diamond growth. *Diamond Relat. Mater.* **2020**, *107*, 107875.
- (31) Yang, J. W.; Park, J. H.; Byun, M. G.; Hwang, N. M.; Park, J.; Yu, B. D. Phonon spectra of clean and Ni-terminated diamond (111) surfaces: An ab-initio study. *Curr. Appl. Phys.* **2021**, *21*, 134–139.
- (32) Hohenberg, P.; Kohn, W. Inhomogeneous electron gas. *Phys. Rev. B* **1964**, *136*, B864–B871.
- (33) Kohn, W.; Sham, L. J. Self-consistent equations including exchange and correlation effects. *Phys. Rev.* **1965**, *140*, A1133–A1138.
- (34) Kresse, G.; Hafner, J. Ab initio molecular dynamics for open-shell transition metals. *Phys. Rev. B: Condens. Matter Mater. Phys.* **1993**, *48*, 13115–13118.
- (35) Kresse, G.; Furthmüller, J. Efficiency of ab-initio total energy calculations for metals and semiconductors using a plane-wave basis set. *Comput. Mater. Sci.* **1996**, *6*, 15–50.
- (36) Perdew, J. P.; Burke, K.; Ernzerhof, M. Generalized gradient approximation made simple. *Phys. Rev. Lett.* **1996**, *77*, 3865–3868.
- (37) Blöchl, P. E. Projector augmented-wave method. *Phys. Rev. B: Condens. Matter Mater. Phys.* **1994**, *50*, 17953–17979.
- (38) Dronskowski, R.; Bloechl, P. E. Crystal orbital Hamilton populations (COHP): energy-resolved visualization of chemical bonding in solids based on density-functional calculations. *J. Phys. Chem.* **1993**, *97*, 8617–8624.
- (39) Deringer, V. L.; Tchougréeff, A. L.; Dronskowski, R. Crystal orbital Hamilton population (COHP) analysis as projected from plane-wave basis sets. *J. Phys. Chem. A* **2011**, *115*, 5461–5466.
- (40) Maintz, S.; Deringer, V. L.; Tchougréeff, A. L.; Dronskowski, R. LOBSTER: A tool to extract chemical bonding from plane-wave based DFT. *J. Comput. Chem.* **2016**, *37*, 1030–1035.
- (41) Park, J. H.; Yang, J. W.; Byun, M. G.; Hwang, N. M.; Park, J.; Yu, B. D. Ab-initio study of the effects of charging on the adsorption and diffusion of Au<sub>2</sub> on MgO(100). *Curr. Appl. Phys.* **2021**, *24*, 39–45.
- (42) Park, J. H.; Yang, J. W.; Byun, M. G.; Hwang, N. M.; Park, J.; Yu, B. D. Charging effects on the adsorption and diffusion of Au adatoms on MgO(100). *J. Phys. Soc. Jpn.* **2021**, *90*, 34602.
- (43) Sung, C.-M.; Tai, M.-F. Reactivities of transition metals with carbon: Implications for the mechanism of diamond synthesis under high pressure. *Int. J. Refract. Met. Hard Mater.* **1997**, *15*, 237–256.



- (44) Häglund, J.; Fernández Guillermet, A.; Grimvall, G.; Körling, M. Theory of bonding in transition-metal carbides and nitrides. *Phys. Rev. B: Condens. Matter Mater. Phys.* **1993**, *48*, 11685–11691.
- (45) Bovenkerk, H. P. Method for production of etched diamond. U.S. Patent 3,083,080 A, 1963.
- (46) Copel, M.; Reuter, M. C.; Kaxiras, E.; Tromp, R. M. Surfactants in epitaxial growth. *Phys. Rev. Lett.* **1989**, *63*, 632–635.
- (47) Tromp, R. M.; Reuter, M. C. Local dimer exchange in surfactant-mediated epitaxial growth. *Phys. Rev. Lett.* **1992**, *68*, 954–957.
- (48) Yu, B. D.; Oshiyama, A. Diffusion and dimer exchange in surfactant-mediated epitaxial growth. *Phys. Rev. Lett.* **1994**, *72*, 3190–3193.
- (49) Yu, B. D.; Miyamoto, Y.; Sugino, O. Efficient n-type doping of diamond using surfactant-mediated epitaxial growth. *Appl. Phys. Lett.* **2000**, *76*, 976–978.
- (50) Wakatsuki, M. New catalysts for synthesis of diamond. *Jpn. J. Appl. Phys.* **1966**, *5*, 337.